Linearity Characteristics of Avalanche Photodiodes For InP Based PICs

Tobias Beckerwerth, Robert Behrends, Felix Ganzer, Patrick Runge, and Martin Schell

***Abstract*—We demonstrate InP PICs with avalanche photodiodes (APD) consisting of InP and InAlAs multiplication regions and investigate these devices regarding their DC and RF linearity characteristics. The optical input dependent gain, bandwidth and output power are characterized and compared to electric field simulations. The space-charge induced electric field reduction is considered to determine the measured properties of the APDs. The APDs with an InAlAs multiplication region exhibit a high bandwidth of 27 GHz in combination with high sensitivity for optical input powers low as 34 μW at a responsivity of 0.65 A/W and a dynamic range of 34 dB. Although the APD with an InP multiplication region shows lower bandwidths of maximum 6 GHz, it demonstrates a high sensitivity for input powers low as 26 μW at a responsivity of 0.85 A/W and a dynamic range of 30 dB making it very attractive for sensing applications. Further, the bias and optical input dependent electric field help to conclude the linearity limitations of the presented devices.**

***Index Terms*—Avalanche photodiode, InP PIC, APD modelling, bandwidth, linearity, RF output power.**

I. Introduction

INTEGRATED PHOTONICS and the development of high performance photonic integrated circuits was driven by telecommunication and its ever increasing demand for higher bit rates. At the receiver end, this was addressed by waveguide integrated high-speed PIN and UTC photodiodes [1], showing high bandwidths and RF output powers [2], [3]. However, these types of photodiodes are intrinsically limited in sensitivity. In contrast, avalanche photodiodes (APDs) can overcome these limitations while sacrificing device bandwidth. In APDs the overall sensitivity of the device benefits by an internal amplification due to an avalanche effect inside the multiplication region with high electric field. The feasibility to integrate lasers or SOAs make InP the most suitable platform for PICs targeting these new applications, e.g., LiDAR, sensing, microwave photonics or quantum communication [4], [5]. While the integration of light sources, modulators, high-speed photodetectors or polarization handling devices has been demonstrated in several InP-based PICs, PICs containing APDs with a high sensitivity for detection of low optical input powers or even single photons have not yet been presented. Especially in PICs for sensing or LiDAR applications, besides the high quantum-efficiency (QE), there is also the need of photodiodes allowing a wide spurious-free dynamic range and the ability to detect weak photon pulses. Waveguide integrated APDs are a promising approach to cover the described needs. Additionally, the integration in a waveguide platform opens the possibility to expand the functionality by integrating other building blocks like multimode interference couplers (MMI), which are suitable for coherent detection schemes [6]. Consequently, the integration of high sensitivity and low noise APDs in an InP waveguide platform enables new applications wide beyond data- and telecommunications [7].

In order to hit all these diverse requirements in sensitivity, bandwidth, dynamic range as well as low noise and the compatibility to integrate light emitting devices, waveguide integrated APDs in an InP platform are investigated. We designed, fabricated and characterized APDs with two different materials for the internal gain causing multiplication and present the results in this article. The devices are fully compatible with our InP foundry process and can be applied to a new branch of InP based PICs, immensely increasing its variety.

II. Design

For both APD structures, the layer stacks are placed on top of waveguide layers including the MMI, which are formed of InGaAsP with a bandgap corresponding to a wavelength of 1.06 μm and InP (see Fig. 1). As a constraint for both APD structures, the n-contact is placed on top of the passive waveguide. Waveguide integrated photodiodes allow to overcome limitations in the trade-off between sensitivity and bandwidth compared to surface-illuminated photodiodes. By the implementation of an evanescently coupling waveguide, the photodiodes layer thicknesses and its mesa dimensions can be reduced and still allowing a high external quantum efficiency (QE). In this way, the carrier transit time, but also the RC time time are minimized.

The epitaxial structure to realize APDs is the separation of the physical properties of the photodiode specifically to discrete layers. This SACM concept (separation of absorption, charge and multiplication) can also be adapted to other material platforms [8], [9]. The structures in this work consist of n- and p-contact layers, an InGaAs absorbing layer, a graded charge layer and two different materials for the multiplication region.

Manuscript received June 16, 2021; revised September 9, 2021 and October 28, 2021; accepted October 29, 2021. Date of publication November 12, 2021; date of current version December 31, 2021.

The authors are with the Photonic Components, Fraunhofer-Institut für Nachrichtentechnik Heinrich-Hertz-Institut, Berlin, Germany (e-mail: tobias.beckerwerth@hhi.fraunhofer.de; robert.behrends@hhi.fraunhofer.de; felix.ganzer@hhi.fraunhofer.de; patrick.runge@hhi.fraunhofer.de; martin.schell@hhi.fraunhofer.de).

Color versions of one or more figures in this article are available at https://doi.org/10.1109/JSTQE.2021.3127853.

Digital Object Identifier 10.1109/JSTQE.2021.3127853

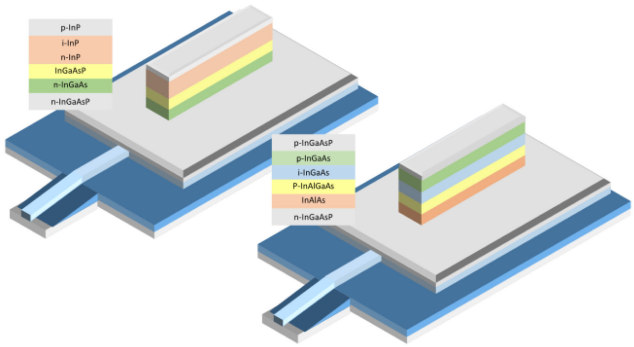

Fig. 1. Schematic of waveguide integrated APDs with InP (left) and InAlAs (right) multiplication layer.

In order to design APDs with high performance, regarding the RF linearity as well as the bandwidth, it is essential to describe and model the carrier transport accurately. Therefore, the electric field distribution and the electric field dependent mobility, as well as the generation rates due to the avalanche effect, need to be properly described. On the epitaxial level, the relation of the potential dependent carrier dynamics needs to be solved. The physics is represented by the Poissons equation:

$$\nabla^2\psi \;=\; -\nabla\tilde{\mathrm{E}} \;=\; \frac{\mathrm{e}}{\varepsilon_{\mathrm{R}}}\left(\mathrm{n}-\mathrm{p}+\mathrm{N}_{\mathrm{A}}^{-}-\mathrm{N}_{\mathrm{D}}^{+}\right) \tag{1}$$

Here ψ represents the electrostatic potential, $\tilde{\mathrm{E}}$ is the electric field with the electron charge e, the local permittivity ε_{R} and the charge densities for free electrons, holes and the acceptor and the donor levels n, p, $+\mathrm{N}_{\mathrm{A}}^{-}$and $-\mathrm{N}_{\mathrm{D}}^{+}$.

In contrast to PIN and UTC photodiodes, where the generation and recombination of carriers is mainly caused in the absorbing region, an additional generation in the multiplication region due to the avalanche effect is considered. The avalanche effect initiating gain is modelled using different models depending on the material. For devices with an InAlAs multiplication layer, the avalanche generation rate $\alpha_{\mathrm{n/p}}$ is described by the Selberherr Model using the coefficients by Goh [10]. It is written for electrons n and holes:

$$\alpha_{n/p} = \; A_{n/p}\exp\;\left[-\left(\frac{B_{n/p}}{E}\right)^{c_{n/p}}\right] \tag{2}$$

The equivalent process of impact ionization in InP is modelled by the formulism derived from Zappa and the used parameter set is given in [11]. This model fits better the measurement characteristics due to the larger multiplication layer thickness used in the InP design. Addtionally, it allows to model high gain characteristics and temperature dependence in order to design APDs for single-photon detection. This description is independent on the multiplication layer thickness and is represented by the following equations.

Independent of the impact ionization description, the drift velocity for electrons $\mathrm{v_e}$ and holes $\mathrm{v_h}$ for all semiconductor compounds are described by the following terms. As adapted in both types of devices, the diffusion time τ_{D} needs also to be considered in partially depleted absorbing regions. The corresponding parameters for InP, InAlAs and InGaAs are given in Table I [12], [13], [14].

TABLE I
MATERIAL PARAMETERS FOR SIMULATION [12], [13], [14]

Symbol		InP	InAlAs	InGaAs
Eg	bandgap	1.35 eV	1.47 eV	0.75 eV
ε_R	permittivity	12.5	12.5	13.8
v_{e_∞}	saturation velocity electr.	0.85 x 10^5 m/s	0.50 x 10^5 m/s	0.75 x 10^5 m/s
v_{h_∞}	saturation velocity holes	-	0.40 x 10^5 m/s	0.48 x 10^5 m/s
μ_e	electron mobility	3500 cm² / Vs	2050 cm² / Vs	8000 cm² / Vs
μ_h	hole mobility	150 cm² / Vs	275 cm² / Vs	300 cm² / Vs
δ	adjustable fit parameter	7.4 10^{-13}	4.9 10^{-12}	7.4 10^{-10}
γ	exp. value	2.5	2.9	3.0
D_e	diffusion constant electr.			200 cm²/s
D_h	diffusion constant holes			25 cm²/s
v_{th}	thermal velocity			0.55 x 10^5 m/s

$$v_e\,(E) \;=\; \frac{\mu_e\;E\;+\;v_e\;\delta\;E^{\gamma}}{1+\;\delta\;E^{\gamma}} \tag{4}$$

$$v_h\,(E) \;=\; v_{h\_\infty}\;tanh\left(\frac{\mu_h\;E}{v_{h\_\infty}}\right) \tag{5}$$

$$\tau_D \;=\; \frac{d^2}{3\;D}+\frac{d}{v_{th}} \tag{6}$$

This parametrization of the field dependent velocity reflects the carrier transport in all segments of the avalanche photodiode for different applied bias voltages, being of special importance for the InGaAs region. For the multiplication region in particular the saturation velocity in high electric fields needs to be set accurately. Taking into account the carrier dynamics as described above, the resulting layer structure was implemented using the commercial Silvaco TCAD drift-diffusion solver. To achieve high responsivities even for thin absorbing regions, an evanescent coupling waveguide structure distributes the incoming light along the APDs mesa length from the waveguide to the absorber. The resulting geometry is solved with a beam propagation method in order to guarantee high coupling efficiency at a wavelength of 1550 nm.

A. *Epitaxial Structure and Band Diagram*

Following the electron-initiated avalanche in InAlAs material, the InAlAs multiplication region is placed to the n-contact, followed by the graded charge layer and a thin absorbing region. The absorbing layer is divided into a p-dopded and an intrinsic part. This concept, known as hybrid absorber, allows to achieve high bandwidths and increases the photodiodes linearity [15]. On top of the absorbing region the p-contact is localized. Equivalently, for the hole initiating InP material, the partially depleted absorbing region is positioned upward of the n-contact. An InGaAsP graded bandgap layer generates a smooth carrier transition to the neighbored InP multiplication layer. All these layers are grown in a single-step metal organic chemical vapor

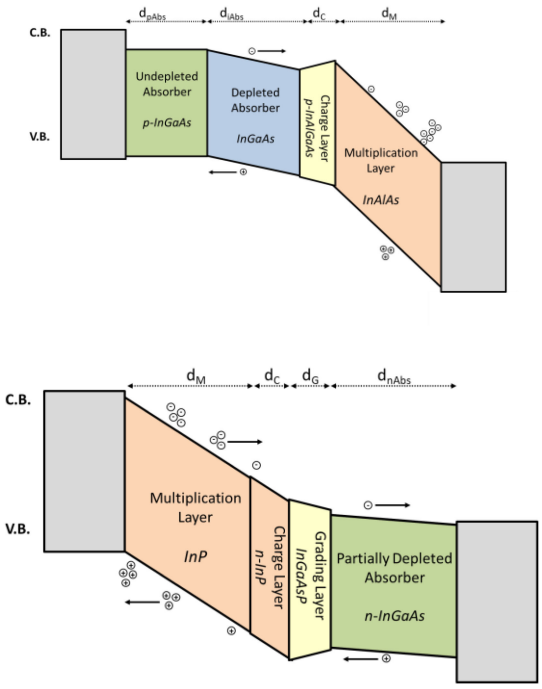

Fig. 2. Band diagram of APD structure with InAlAs (top) and InP multiplication layer (bottom).

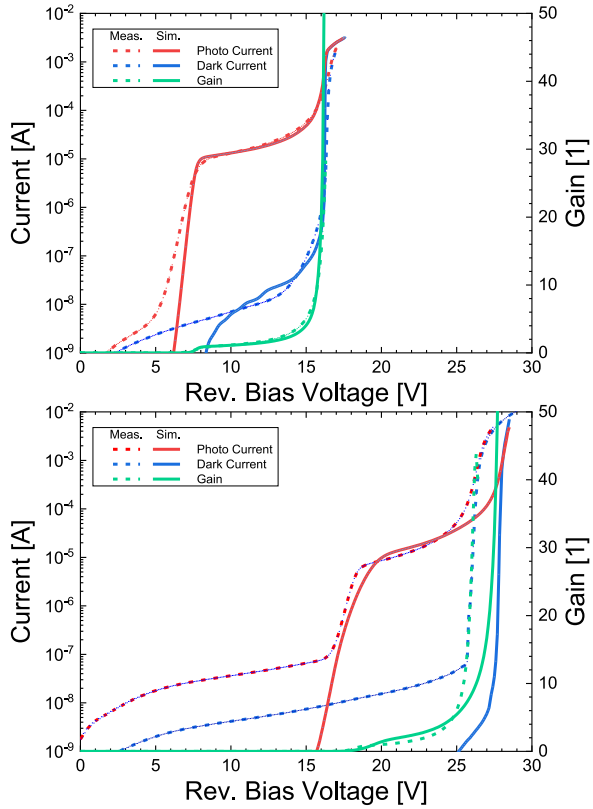

Fig. 3. Measurement and simulation of IV characteristics and gain for different APDs with an InAlAs (top) and InP (bottom) multiplication layer.

phase epitaxy (MOVPE). The band diagrams for these layer stacks are presented in Fig. 2. Consequently, the electrons, which are the minority carriers in the absorbing region of the InAlAs design, experience a fast carrier diffusion from the undepleted layer into the depleted layer, where the drift velocity dominates the carrier transport. When continue drifting into the multiplication region the bandgap graded charge layer guarantees a fast carrier transport due to smoothening the band energies. The charge doping controls the electric field strength in the adjoining intrinsic regions. In contrast, in the InP multiplication layer design, the avalanche is initiated by holes, diffusing from the partially depleted absorbing layer in to the InP region. According to formula (6), this carrier transit time in the n-doped InGaAs layer is limiting the device bandwidth. As a benefit of the doping, the electric field remains low in the InGaAs layer, resulting in very low dark current.

III. DC AND RF CHARACTERIZATION

A. DC Characteristics

The fabricated devices have been characterized regarding their DC and RF performance. In order to evaluate the DC characteristics, first the dark current was measured. Further, the photo current at an optical input power of 50 µW and the corresponding gain properties were determined. While a thinner multiplication region for the InAlAs based device yields a low breakdown V_{Br} voltage of below 17 V, it shows a high dark current of 1 µA close to at a voltage of 16 V (see Fig. 3), being 95% of the breakdown voltage V_{Br}. The APD show a suitable operation point in terms of gain, dark current and bandwith at 16 V, but are not restricted to be operated in this voltage regime. The high dark current at 16 V is to our knowledge induced from the relative high electric field in the hetero-junction of the absorbing low bandgap InGaAs layer and the adjacent InAlGaAs layer as well as the high electric field strength at the edge of the mesas sidewall (see Fig. 4). By measuring the photo current, the gain was normalized to the current at the beginning of the plateau, where the IV curve is flattening out after a sharp rise. This corresponds to a full depletion of APD and a minimum gain, defined as unity gain. Due to a high electric field in

$$\alpha_{n/p} = \frac{qE}{E_{th}^{n/p}} \exp\left\{0.217\left(\frac{E_{th}^{n/p}}{E_R^{n/p}}\right)^{1.14} - \left[\left(0.217\left(\frac{E_{th}^{n/p}}{E_R^{n/p}}\right)^{1.14}\right)^2 + \left(\frac{E_{th}^{n/p}}{qE\lambda_{n/p}}\right)^2\right]^{0.5}\right\}$$

$$\text{where } \lambda_{n/p} = B_Z^{n/p} \tanh\left\{\frac{C_Z^{n/p}}{2kT}\right\} \text{ and } E_{n/p} = D_Z^{n/p} \tanh\left\{\frac{E_Z^{n/p}}{2kT}\right\} \quad (3)$$

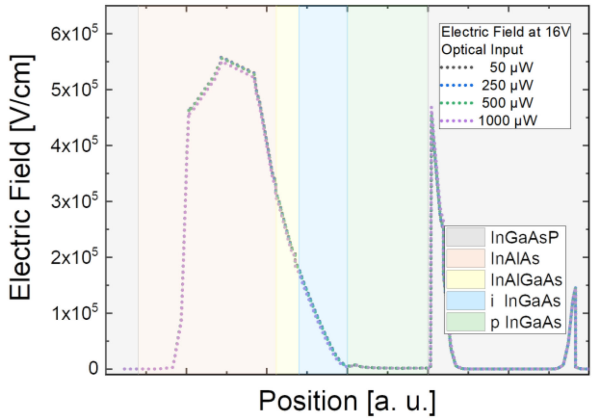

Fig. 4. Electric field distribution of APD with InAlAs multiplication layer at a reverse bias of 16 V.

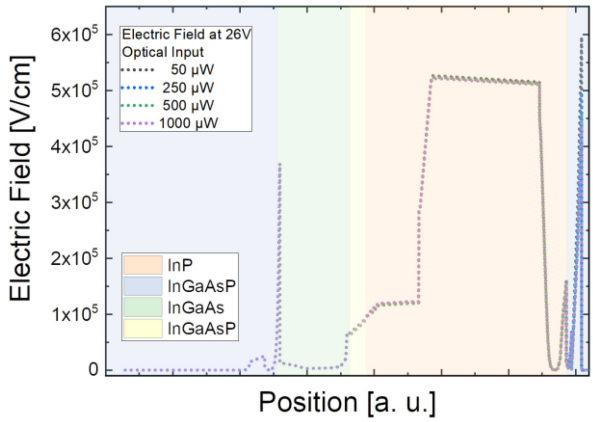

Fig. 5. Electric field distribution of APD with InP multiplication layer at a reverse bias of 26 V .

the multiplication region, the effective gain for the fabricated devices at this voltage is allready slightly larger than 1 ($M > 1$). This can be observed in a slope of the photo currents at voltages at unity gain and affects the responsivity at this voltage. For the InAlAs design, the corresponding voltage V_{M1} was found to be 9 V at a responsivity of 0.65 A/W. This represents an external quantum efficiency, including all coupling losses, of 52% with a mesa dimension of 5x20 µm^2. For a low optical input power the derived gain is up to $M = 25$.

The design with an InP multiplication layer shows a higher breakdown voltage V_{Br} of 27 V and a maximum gain of $M = 40$, while the dark current is still below 60 nA at a reverse bias voltage of 25.5 V, representing 95% V_{Br} (see Fig. 3). This low dark current is going along with a lower electric field in the low bandgap material, but also resulting from a lower defect density in the growth of InP material compared to InAlAs.

The simulated electric field distribution of the InP design at a reverse bias voltage of 26 V is presented in Fig. 5. The measured IV characteristics is in agreement with the simulated results, proving the robustness of the methodology.

For this APD design, the unity gain voltage is 19 V, and the responsivity is 0.85 A/W corresponding to 68% external QE with a mesa dimension of 4x50 µm^2. The electric field at a reverse bias voltages close to the breakdown voltage as well as the DC properties have been simulated for different input powers to reflect the dominating physics at high optical input powers. It is remarkable, that in undepleted or partially depleted InGaAs regions, the carriers are crossing the layer within the diffusion time τ_D. This diffusion time strongly depends on the carrier type, but not linear in the thickness in contrast to the transit time described by the drift velocity. Consequently, the total thickness of the partially depleted and undepleted absorber, as well as the type of minorities due to doping of the InGaAs is crucial to achieve high-speed performance. Moreover, the carrier transit of electrons in the InP based design as well as the carrier transit of holes in the InAlAs design are essential for the linearity of the fabricated devices. When the optical input power is increased, more electron-hole pairs are generated, yielding to more carriers initiated in the multiplication region to trigger the avalanche cascade. This leads also to an accumulation of secondary carriers, which are electrons for the InP and holes for InAlAs design.

These carriers induce a space charge, reducing the electric field in the multiplication region (see Figs. 4 and 5). In the wider InP multiplication region, the maximum electric field, but also the gain decreasing field reduction are lower compared to the design with a InAlAs multiplication layer. The reduction of the electric field strength in the multiplication region can also be observed in the reduced gain, which is directly measured for different input powers (see Fig. 6). The simulation of the gain characteristics is more accurate for the InAlAs design, but the same effect of a reduced field in the multiplication region can be reflected for both APD types. Referred to equation 2 and 3, the slight change of the electric field impacts strongly the impact ionization rate. As a result, the simulated gain is reduced at high optical inputs matching the simulation results.

B. RF Performance

To conclude the dominating mechanisms in the RF performance of the fabricated devices, the bandwidth as well as the RF output power at a variable optical input have been measured for different reverse bias voltages. The measured relative s_{21} parameter are shown in Fig. 7. As it can be observed in Fig. 7 (top), for an optical input power of 50 µW the InAlAs design demonstrates a bandwidth of 27 GHz at low reverse bias voltages up to 13 V and a gain of $M = 2$. When increasing the bias voltage to 14 V and 15 V, the bandwidth slightly decreases to 25 GHz and 24 GHz, respectively, while the gain rises from $M = 3$ to $M = 5$. At a reverse bias voltage of 16 V, the measured bandwidth is determined with 19 GHz and a gain of $M = 12$. This effect results from the increasing avalanche build-up time, which strongly depends of the drift of secondary slow holes in the intrinsic depleted absorbing region.

In the InP based design, where secondary generated electrons pass into the partially depleted absorber, the fast diffusion of minorities is taking place. Consequently, the dominating limitation of the bandwidth is not the avalanche build-up time, but the diffusion of the slow holes before passing into the multiplication

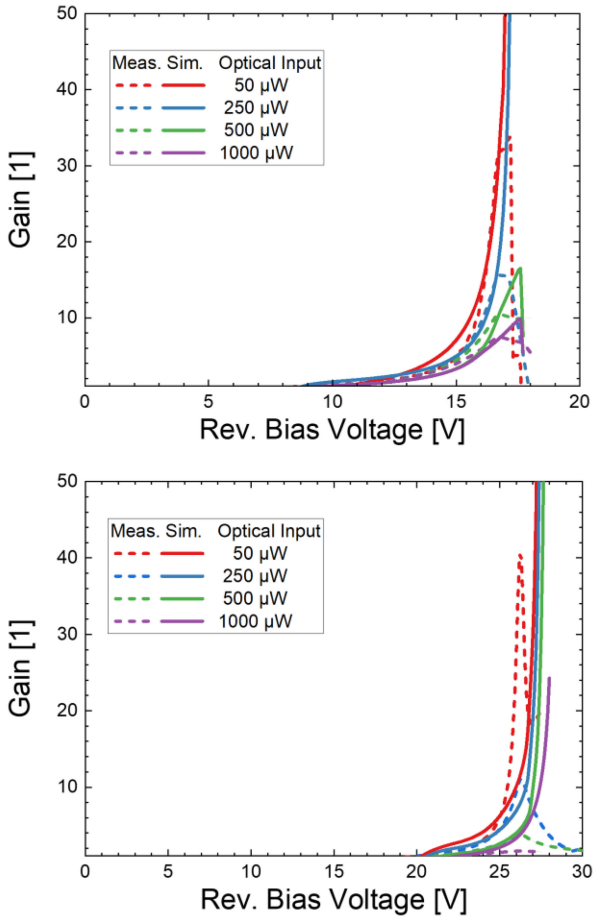

Fig. 6. Measurement and simulation of gain characteristics for different input powers for the APD with InAlAs (top) and InP (bottom) multiplication layer.

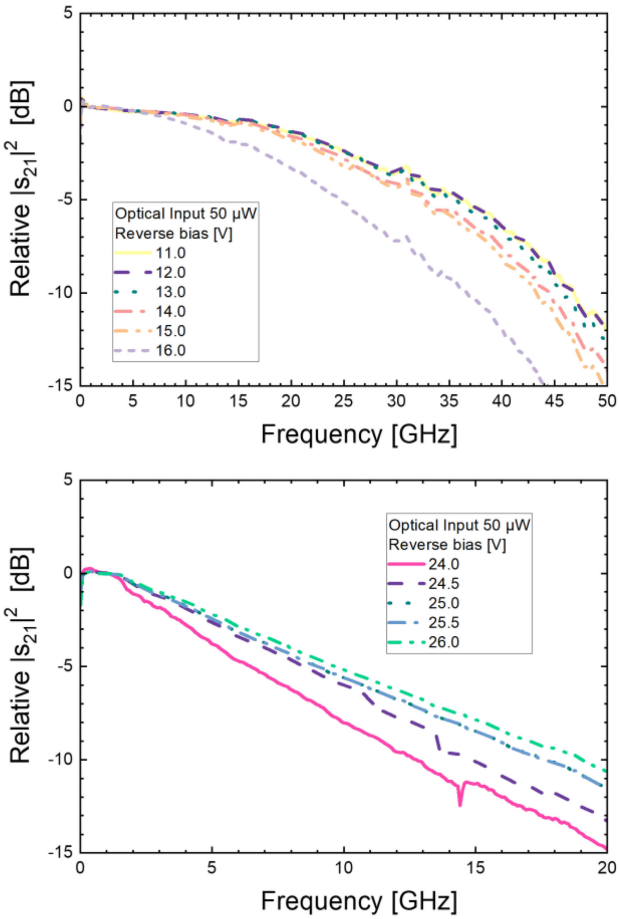

Fig. 7. RF bandwidth measurement for APD with InAlAs (top) and InP (bottom) multiplication layer at different bias voltages.

region. Hence, the 3dB-bandwidth even increases with the bias voltage up to 26 V to 6 GHz and a gain of M = 11 (see Fig. 7).

C. Linearity Characteristics

For each of the characterized devices, the RF output power was evaluated at a carrier frequency close to the 3dB-bandwidth. For the APD with the InAlAs avalanche layer, the carrier frequency was set to 20 GHz and the applied reverse bias voltage was incrementally adjusted from 10 V to 16 V (see Fig. 8). From 10 V to 14 V, the observed characteristics are very similar. In the range of a photo current from 100 µA up to 5mA, the RF power increases linearly up to a total power of -6 dBm. The slope is related to the product of effective avalanche gain M and the quantum efficiency QE. As we can see, at higher reverse bias voltages of 15 V and 16 V (Fig. 8 top), when the gain is increased, also the RF power increases at a steeper slope up to a photo current of 3 mA. At higher photo currents, referring to more optical input power, the higher gain at 16 V is compensated by the space-charge induced electric field reduction as described in Section III a. The reduced gain then results in a similar slope for all applied voltages at photo currents above 3 mA. However, the maximum RF output power is lower at higher voltages, but achieved with lower optical input power.

A real benefit of the linear avalanche mode is the increased sensitivity and a wide dynamic range. The total dynamic range from -40 dBm to -6 dBm covers 34 dB. Assuming the measured external QE of 50% and a gain of M = 2, the corresponding minimum photocurrent is 100 µA at an optical input power of 100 µW. At a voltage of 16 V, the minimum photocurrent is 170 µA at a Gain of M = 10, which relates to a minimum input power of 34 µW. Consequently, the lowest optical input is reduced.

This advantage can be observed for the InP design as well. The minimum photocurrent is 50 µA at a gain of M = 2. Considering the QE of 68%, the minimum optical input power is determined to be 37 µW. At a reverse bias voltage of 26 V and a gain of M = 11, the photocurrent of 200 µA is converted from an optical input power of 26 µW. The dynamic range, reaching from -42 dBm to -12 dBm is 30 dB. Different from the design with the InAlAs multiplication region, here the maximum RF output power is achieved for the highest investigated reverse bias voltage. This is in accordance with the bandwidth measurement, also increasing with the applied reverse bias voltage due to the low transit time of secondary electrons. Similar to the InAlAs design, the converted RF power increases at higher voltages at a steeper slope for photo currents below 1 mA and aligns for photo currents above 1 mA. This is in accordance with the reduction of the reduced DC gain at higher optical input powers. The maximum saturation current

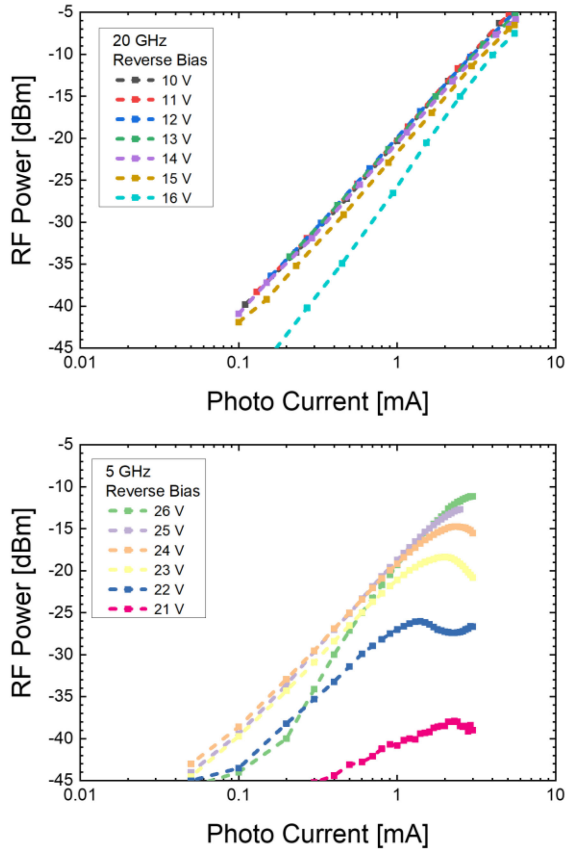

Fig. 8. RF power for APD with InAlAs (top) and InP (bottom) multiplication layer at different bias voltages.

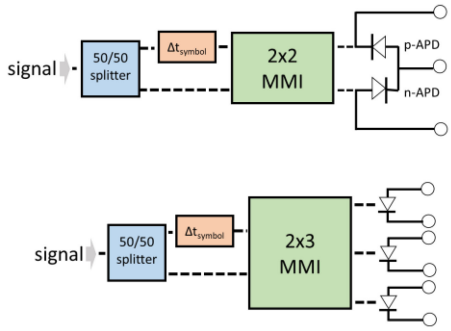

Fig. 9. Device configuration with MMI coupler for self-coherent detection.

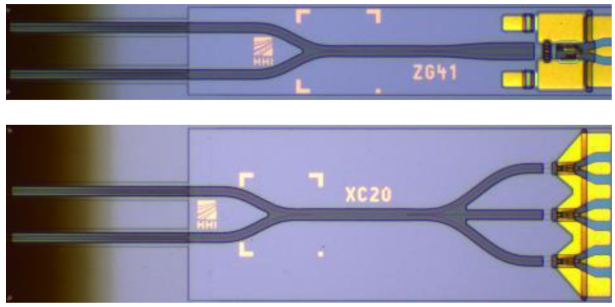

Fig. 10 Fabricated InP PIC with 2x2 MMI and balanced APD for heterodyne coherent detection (top) and 2x3 MMI with triple APD for homodyne coherent detection (bottom).

is 3 mA. We also do observe the potential to achieve even higher photo currents as for the measurement at 22 V reverse bias. At a maximum RF power of -26 dBm, a higher photo current leads to a lower RF power. Due to the reduced gain of the APD, the conversion efficiency changes and thereby the slope in Fig. 3. This can be compensated by a higher optical input. While the RF power is increasing for higher optical inputs, it does not exceed the maximum output power of -25.8 dBm.

Regardless the lower bandwidth and the dynamic range, the low dark current and the high sensitivity of the InP device make it very attractive for sensing applications. For surface illuminated APDs the larger effective area can compensate higher input powers due to a decrease optical density, yielding to higher photocurrents and absolute higher RF output powers [16].

However, the dynamic range of waveguide integrated APDs can exceed more than 30 dB for InAlAs and InP based designs. As discussed, when the applied bias voltage is increased, the gain and thus the ratio of RF power and photocurrents arises up to a critical photocurrent. Beyond that photocurrent, the gain reduction is correlated with an aligned slope for the RF power at all applied reverse bias voltages. In other photodiodes, e.g., PIN or UTC, the space-charge effect can easily be compensated by increasing the bias voltage. In this way, the maximum RF power can be increased. Similar to [17] for the demonstrated PIC based APDs, the change of the bias voltage has a strong impact on the gain characteristics due to the field reduction in the multiplication region. Even, if the maximum RF power can not be exceeded at higher bias voltages, it improves the sensitivity and thus the minimum optical input power.

IV. PICs and Applications

Besides the fabrication of single photodiodes, the presented APDs have been combined with different MMI couplers and spotsize converters for the realization of advanced photodetector PICs. These photodetector PICs, for example consisting of balanced APDs and a 2x2 MMI and can be used for self-coherent detection.

Therefore, one input of the MMI is extended with a delay line by $\Delta t_{\mathrm{symbol}}$ and a 50/50 splitter divides the incoming Rx signal (see Fig. 9). The differential phase in between two symbols is detected using a pair of high sensitive photodiodes. The waveguide integrated APDs enable the self-coherent detection scheme, which was always lacking of insufficient sensitivity. As a result, highly sensitive coherent detection without a local oscillator is achievable. Instead of using the classical approach of a 90° optical hybrid for homodyne detection, a simplified version with a 120° optical hybrid, realized as a 2x3 MMI in combination with three photodiodes can be used (see Fig. 9), having the advantage of wider optical bandwidth from L- to C-band [18]. Both of these advanced configurations for photodetector PICs have been fabricated, except the delay line and the 50/50 splitter (see Fig. 10). Exemplary, a simple version of a heterodyne photodetector PIC with a balanced APD chip and a 2x2 MMI has been characterized. The APDs responsivities and the common-mode rejection ratio (CMRR) over the C-band

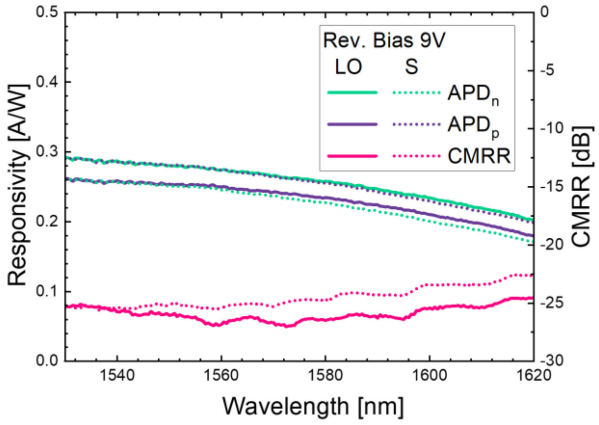

Fig. 11. Measured external responsivity and CMRR of PIC with 2x2 MMI and balanced InAlAs APDs at the two inputs for local oscillator (LO) and signal (S).

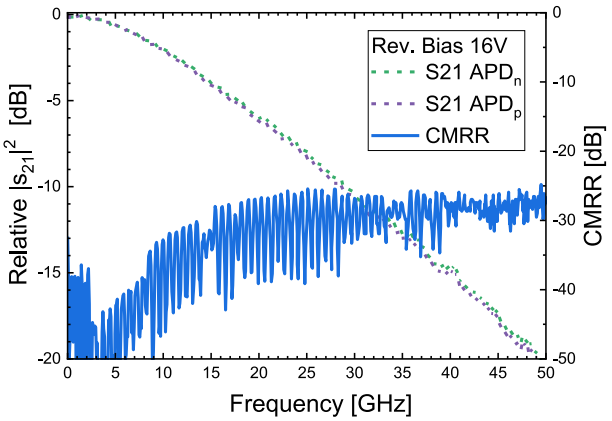

Fig. 12. Measured S21 and CMRR of PIC with InAlAs APDs and 2x2 MMI at an optical input of 50 µW.

have been measured at unity-gain (see Fig. 11) to evaluate the uniformity of the PIC. The external responsivity at 1550 nm is above 0.26 A/W for both APDs, resulting from the 3 dB splitting within the MMI and an additional loss of 17% within the MMI.

Further, the bandwidth and the CMRR at an operation voltage of 16 V are evaluated for the independently measured output power P_{S21_n} and P_{S21_p} of the corresponding photodiodes (see Fig. 12). Compared to the single devices, the bandwidth is reduced to 14 GHz due to an increased RC delay of these devices. The CMRR drops below -15 dB for frequencies up to 5 GHz. Beyond 5 GHz the small-signals of the two measured APDs differentiate much stronger, leading to a lower CMRR of -10 dB. Although the performance can be improved future iterations, this PIC proves the ability for coherent detection with low optical input powers. The demonstrated devices allow the reception of high modulation formats and are applicable for telecommunication, sensing or FMCW LiDAR.

V. Conclusion

We demonstrated two types of waveguide integrated avalanche photodiodes with InP and InAlAs multiplication regions and investigated their different characteristics including gain, bandwidth and output power. The devices show bandwidths of up to 27 GHz / 6 GHz, high saturation currents of 5 mA / 3 mA for the design with InAlAs / InP, respectively. In accordance with the gain measurements for different photocurrents, the space-charge induced reduction of the electric field was modelled and its impact on the limitation for the DC gain and the RF linearity are described.

The fabricated APDs with an InAlAs multiplication show an excellent RF performance with a high bandwidth of 27 GHz and a wide dynamic range of 36 dB at 20 GHz. The determined minimum input power is 34 µW. This makes it attractive for integrated photodetector circuits in high-speed applications. Next to the good RF performance, the waveguide integration enables the fabrication of small mesa sizes to reduce the dark current contributions. The InP design shows a bandwidth of 6 GHz and a dynamic range of 30 dB at 5 GHz. While the InP based APDs do not target high-speed applications, their low dark current and the high sensitivity for optical input powers below 26 µW can be applied for photodetector PICs in sensing applications or LiDAR. Due to the waveguide integrated APDs, self-coherent detection schemes become attractive, because of avoiding local oscillators and still allowing highly sensitive coherent detection.

References

[1] E. Rouvalis *et al.*, "High-speed photodiodes for InP-based photonic integrated circuits," *Opt. Exp., vol.*, vol. 20, pp. 9172–9177, 2012.
[2] F. M. Soares *et al.*, "InP-Based foundry PICs for optical interconnects," *Appl. Sci.*, vol. 9, no. 8, 2019, Art. no. 1588. doi: https://doi.org/10.3390/app9081588.
[3] P. Runge *et al.*, "Waveguide integrated balanced photodetectors for coherent receivers," *IEEE J. Sel. Topics Quantum Electron.*, vol. 24, no. 2, Mar./Apr. 2018, Art. no. 6100307, doi: 10.1109/JSTQE.2017.2723844.
[4] S. Arafin and L. A. Coldren, "Advanced InP photonic integrated circuits for communication and sensing," *IEEE J. Sel. Topics Quantum Electron.*, vol. 24, no. 1, Jan./Feb. 2018, Art. no. 6100612, doi: 10.1109/JSTQE.2017.2754583.
[5] B. J. Isaac, B. Song, S. Pinna, L. A. Coldren, and J. Klamkin, "Indium phosphide photonic integrated circuit transceiver for FMCW LiDAR," *IEEE J. Sel. Topics Quantum Electron.*, vol. 25, no. 6, Nov./Dec. 2019, Art. no. 8000107, doi: 10.1109/JSTQE.2019.2911420.
[6] H. Zhao *et al.*, "High-power indium phosphide photonic integrated circuits," *IEEE J. Sel. Topics Quantum Electron.*, vol. 25, no. 6, Nov./Dec. 2019, Art. no. 4500410, doi: 10.1109/JSTQE.2019.2908788.
[7] P. Runge *et al.*, "Polarisation insensitive coherent receiver PIC for 100Gbaud communication," in *Proc. Opt. Fiber Commun. Conf.*, 2016, pp. 1–3.
[8] N. J. D. Martinez *et al.*, "High performance waveguide-coupled Ge-on-Si linear mode avalanche photodiodes," *Opt. Exp.*, vol. 24, pp. 19072–19081, 2016.
[9] M. Huang *et al.*, "56GHz waveguide Ge/Si avalanche photodiode," in *Proc. Opt. Fiber Commun. Conf. Expo.*, 2018, pp. 1–3.
[10] Y. L. Goh *et al.*, "Avalanche multiplication in InAlAs," in *IEEE Trans. Electron Devices*, vol. 54, no. 1, pp. 11–16, Jan. 2007, doi: 10.1109/TED.2006.887229.
[11] F. Zappa, P. Lovati, and A. Lacaita, "Temperature dependence of electron and hole ionization coefficients in InP," in *Proc. 8th Int. Conf. Indium Phosphide Related Mater.*, 1996, pp. 628–631, doi: 10.1109/ICIPRM.1996.492327.
[12] W.-P. Hong *et al.*, "Material properties and clustering in molecular-beam epitaxial $In_{0.52}Al_{0.48}As$ and $In_{1-x-y}Ga_xAl_yAs$," Diss. American Vacuum Society, 1987.
[13] M. Dentan and B. de Cremoux, "Numerical simulation of the nonlinear response of a p-i-n photodiode under high illumination," *J. Lightw. Technol.*, vol. 8, no. 8, pp. 1137–1144, Aug. 1990, doi: 10.1109/50.57833.
[14] K. Brennan and K. Hess, "Theory of high-field transport of holes in GaAs and InP," *Phys. Rev. B*, vol. 29, May 1984, Art. no. 5581.

[15] M. Nada, Y. Muramoto, H. Yokoyama, T. Ishibashi, and H. Matsuzaki, "Triple-mesa avalanche photodiode with inverted P-down structure for reliability and stability," *J. Lightw. Technol.*, vol. 32, pp. 1543–1548, 2014.
[16] H. Zhao *et al.*, "High-speed avalanche photodiodes with wide dynamic range performance," *J. Lightw. Technol.*, vol. 37, pp. 5945–5952, 2019.
[17] Z. Ahmad *et al.*, "Avalanche photodiodes with dual multiplication layers and ultra-high responsivity-bandwidth products for FMCW Lidar system applications," *IEEE J. Sel. Topics Quantum Electron.*, vol. 28, no. 2, Mar./Apr. 2022, Art. no. 3800709, doi: 10.1109/JSTQE.2021.3062637.
[18] P. Runge *et al.*, "Monolithic integrated InP receiver chip for coherent phase sensitive detection in the C- and L-band for colorless WDM applications," in *Proc. Eur. Conf. Opt. Commun.*, 2014, pp. 1–3, doi: 10.1109/ECOC.2014.6963858.

Tobias Beckerwerth was born in 1987 in Pritzwalk, Germany. He received the B.Sc. degree from Freie Universität Berlin, Berlin, Germany, in 2012 and the M.Sc. degree from Technische Universität Berlin, Berlin, in 2015, both in physics. Since 2015, he has been with Photonic Components Department, Fraunhofer Heinrich Hertz Institute, Berlin, and is currently working toward the Ph.D. degree. His research focuses on the development of photodetectors in InP technology.

Robert Behrends, photograph and biography not available at the time of publication.

Felix Ganzer, photograph and biography not available at the time of publication.

Patrick Runge received the Dipl.-Ing. degree in computer science and the Ph.D. degree in electrical engineering from the Technical University of Berlin, Berlin, Germany, in 2005 and 2010, respectively. From 2005 to 2007, he was with Hymite GmbH, where he was involved in the RF design and measurement of optoelectronic packages for optical communication. In 2007, he returned to the Technische Universität Berlin, to pursue the Ph.D. degree, where he investigated nonlinear effects and applications of ultralong semiconductor optical amplifiers. After finishing his Ph.D. degree, he worked from 2010 to 2011 for a patent attorney. Since 2011, he has been with Fraunhofer Heinrich Hertz Institute (HHI), Berlin, Germany, where he is engaged in the development and fabrication of photodetectors and photonic integrated circuits based on InP. He is currently the Head of Detector Group, Photonic Components Department, HHI. Since 2020, he has been an Associate Editor for the IEEE/OSA JOURNAL OF LIGHTWAVE TECHNOLOGY. Since 2014, he has been a Member of ECIO Steering Committee and serves frequently for conference subcommittees, such as, CSW-IPRM, OSA APC.

Martin Schell received the Dipl.-Phys. degree from RWTH Aachen, Aachen, Germany, in 1989 and the Dr. rer. nat. degree from the Technische Universität Berlin, Berlin, Germany, in 1993. He is currently a Professor of optic and optoelectronic integration with the Technical University of Berlin, and the Director of Fraunhofer Heinrich Hertz Institute, Berlin. He is a Board Member of European Photonics Industry Consortium (EPIC), a Board Member of OptecBB (Competence Network Optical Technologies Berlin/Brandenburg), a Member of the Photonics21 Board of Stakeholders, and a Member of Public Policy Committee of the Optical Society of America. From 2000 to 2005, he was first a Product Line Manager, and then the Head of production and procurement, Infineon Fiber Optics, Munich, Germany. From 1996 to 2000, he was a Management Consultant with Boston Consulting Group, Boston, MA, USA. Before that, he spent one year as a Visiting Researcher with Tokyo University, Tokyo, Japan.